Evaluation of RF Through-The-Wall Mapping Reconstruction Methods using an Objective Image Quality Index

Rafael Saraiva Campos, Lisandro Lovisolo and Marcello L. R. de Campos

***Abstract*— This work aims at comparing four reconstruction techniques (Filtered Backprojection Reconstruction, Direct Fourier Reconstruction, Algebraic Reconstruction Technique and Simultaneous Iterative Reconstruction Technique) that can be applied to RF-based through-the-wall mapping. All these methods were originally used in computerized X-ray tomography. A stochastic simulation model is set up, using pathloss equations corrupted by Rayleigh noise to account for multipath reception of the RF wave and two test floor maps are defined. From that analysis, a metric for image quality assessment (Mean Structural Similarity Index) is selected to allow an objective comparison of the reconstructed images.**

***Keywords*— through-the-wall mapping, Radon projection, parallel-beam geometry, backprojection, algebraic reconstruction**

I. Introduction

Indoor positioning techniques allow locating and tracking RF mobile devices, which can improve tactical situation awareness in critical conditions, such as search-and-rescue and military operations in urban areas [1]. Situation awareness in a tactical level is the perception of environmental variables, in time and space, and the ability to understand and interrelate them, as a basis for quick decision making in crisis intervention [2]. Situation awareness can be further improved by techniques such as Through-the-Wall Mapping (TWM). It aims at mapping static obstacles without sensing them directly. Thus, it provides a non-invasive way to build a floor map. TWM floor map reconstruction can be treated as a discrete inverse problem [3], and employs algorithms originally applied to X-ray Computerized Tomographic Imaging (CTI) [4].

This work focuses on RF-based TWM under a parallel-beam acquisition geometry, such as the one depicted in Fig. 1. We define a stochastic simulation model and select an objective metric to evaluate and compare four different reconstruction algorithms largely used in CTI [5]: (i) Filtered Backprojection Reconstruction (FBR) [6];(ii) Direct Fourier Reconstruction (DFR) [6]; (iii) Algebraic Reconstruction Technique (ART) [5]; (iv) Simultaneous Iterative Reconstruction Technique (SIRT) [7].

The remainder of this work is organized as follows: Section II defines the RF-based TWM simulation model and its parameters; Section III explains the selection of an objective comparison metric for the evaluation of the reconstructed images quality; Section IV analyzes the simulation results. Finally, Section V draws a brief conclusion.

Rafael Saraiva Campos (CEFET/RJ), Lisandro Lovisolo (PROSAICO/PEL/DETEL/UERJ), Marcello L. R. de Campos (PEE/COPPE/UFRJ). E-mails: rafael.campos@cefet-rj.br, lisandro@uerj.br, campos@smt.ufrj.br.

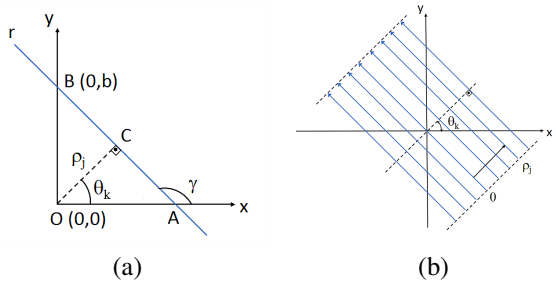

(a) (b)

Fig. 1. (a) Defining the line equation using polar parameters ρ and θ; (b) Parallel-ray beam for $\theta = \theta_k$.

II. Problem Model

In the absence of data from field measurements, one has to resort to computer simulations to evaluate reconstruction algorithms applied to RF TWM. These simulations typically rely on empirical path loss equations (offset-slope models). These propagation models apply the geometric optics approximation, i.e., they disregard common wave propagation phenomena such as diffraction. Furthermore, they also do not take into account ray bending due to refraction and multipath reception caused by multiple reflections, i.e., these models assume single-path straight-line propagation. Rician or Rayleigh distributions are commonly used to provide an additional random path loss component [8] to take the effect of multipath into consideration. Floor blueprints are provided, so that the reconstruction techniques can be evaluated.

A. Propagation Modeling

Referring to the parallel-beam geometry depicted in Fig. 1, one describes the mean received power P_r (dBm) at d meters from the transmitter along the line defined by (ρ_j, θ_k), $j = 1, \ldots, m$ and $k = 1, \ldots, n$ by means of

$$P_r(\rho_j, \theta_k) = P_t - L_t + G_t - L_d - \sum_i \alpha_i(\rho_j, \theta_k) l_i(\rho_j, \theta_k) + G_r - L_r \quad (1)$$

where $l_i(\rho_j, \theta_k)$ and $\alpha_i(\rho_j, \theta_k)$ are the length (meters) and the attenuation factor (dB/m) across the ith obstacle, respectively. P_t (dBm) is the mean transmitted power. L_t and L_r are the losses (dB) due to cables and connections at the transmitter and receiver, correspondingly. G_t and G_r are the transmitter and receiver antennas gains (dBi), in that order. L_d is the

propagation loss (dB) as a function of the transmitter-receiver distance (d).

Equation (1) represents the path loss assuming single-path straight line propagation. In such a scenario, it is clear that

$$\sum_i \alpha_i(\rho_j, \theta_k) l_i(\rho_j, \theta_k) = g(\rho_j, \theta_k) \quad (2)$$

i.e., the summation of the losses across the obstacles along the line defined by (ρ_j, θ_k) is equal to the Radon transform [6] of the floor blueprint $f(x, y)$ along that same line. This comes from the very definition of the Radon transform. Thereby, equation (1) can be rewritten as

$$g(\rho_j, \theta_k) = P_t - P_r(\rho_j, \theta_k) - L_t - L_r - L_d + G_t + G_r \quad (3)$$

Therefore, by measuring $P_r(\rho_j, \theta_k)$ for $j = 1, \ldots, m$, one obtains the Radon projection $g(\rho, \theta_k)$ of $f(x, y)$ at angle θ_k.

The value of L_d (dB) can be approximated by an empirical model, such as the one defined by

$$L_d = \beta_{\text{offset}} + \beta_{\text{slope}} \log\left(\frac{d}{d_0}\right) \quad (4)$$

where β_{offset} is the propagation loss (dB) at a distance d_0 meters from the transmitter, and β_{slope} is the path loss exponent or slope (dB/decade). Calibration campaigns are required to fine tune such models before they can be applied to a specific environment. During these campaigns, at each selected measurement point, the distance d and the mean propagation loss at that location are registered. Then, linear regression can be used to estimate β_{offset} and β_{slope} [9]. Along a d-meter path, the ray passes through two environments: outside and inside the floor being mapped. If d is the transmitter-receiver distance, $d_{\text{in}}(\rho_j, \theta_k)$ is the distance traversed inside the floor by the ray defined by (ρ_j, θ_k), and assuming $d_0 = 1$ meter, equation (4) becomes $L_d(\rho_j, \theta_k) = \beta_{\text{offset}} + \beta_{\text{slope,out}} \log\left(\frac{d}{d_{\text{in}}(\rho_j, \theta_k)}\right) + \beta_{\text{slope,in}} \log\left(d_{\text{in}}(\rho_j, \theta_k)\right)$, where $\beta_{\text{slope,in}}$ and $\beta_{\text{slope,out}}$ are the slope inside and outside the floor, respectively.

B. Maximum Supportable Over-the-Air Path Loss

The maximum supportable over-the-air path loss (dB) is given by

$$L_{\text{max}} = \text{EIRP} + G_r - L_r - S_0 \quad (5)$$

where S_0 is the receiver sensitivity (dBm); the Effective Isotropic Radiated Power (EIRP) in dBm is defined by

$$\text{EIRP} = P_t - L_t + G_t \quad (6)$$

Using equations (5) and (6) to replace the proper terms in equation (3), one gets $g(\rho_j, \theta_k) = L_{\text{max}} + S_0 - P_r(\rho_j, \theta_k) - L_d(\rho_j, \theta_k)$.

Any received signal below S_0 is reported as equal to S_0, i.e., $P_r(\rho_j, \theta_k) \geq S_0$. As a result, the maximum detectable shadowing loss along the path defined by (ρ_j, θ_k) is $g_{\text{max}}(\rho_j, \theta_k) = L_{\text{max}} - L_d(\rho_j, \theta_k)$. Thereby, during the acquisition of the RF samples, the Radon projection is effectively "clipped" at $g_{\text{max}}(\rho_j, \theta_k)$. This means that information about the obstacles along the propagation path is lost, which will result in additional reconstruction error.

C. Static Multipath Propagation

In the acquisition phase, the transmitter-receiver pair is static during the measurements at each position. The intervening obstacles are also not moving in relation to the transmitter-receiver pair. Therefore, multiple reflections at the walls and diffraction result in static multipath fading. Such condition is deterministic, and given enough information about the environment – which is not available when one intends to map a floor – it would be possible to estimate the several propagation paths using ray-tracing techniques. Static multipath reception alters the shadowing loss estimates, which has a direct effect on the reconstruction error. The effect of multipath in stationary links can be modeled by a Rayleigh distribution. The random values selected from this distribution provide the additional propagation loss, to be added to the previously calculated average propagation loss (path loss plus shadowing). As no ray-tracing techniques are used, one might assume that the multipath components (amplitude and phase) are random, but that their average is time-invariant, for any given transmitter-receiver path through the target floor [8]. Equation (2) then becomes

$$g(\rho_j, \theta_k) = \sum_i \alpha_i(\rho_j, \theta_k) l_i(\rho_j, \theta_k) + \Delta_b \quad (7)$$

where Δ_b(dB) is the multipath fading relative to the mean received power, given by $\Delta_b = 20 \log_{10}\left(\frac{R_b}{2b}\right)$, where R_b is the Rayleigh probability distribution function with parameter b, defined by $R_b = \frac{x}{b^2} e^{\left(\frac{-x^2}{2b^2}\right)}$, where x is the received signal amplitude, and b is equal to half the average received signal amplitude, i.e, $b = \frac{1}{2}\sqrt{10^{[0.1(P_t - L_t + G_t - L_d + G_r - L_r)]}}$.

Equation (7) indicates that the Radon projection along the direction defined by ρ_j and θ_k is equal to the shadowing loss through the obstacles along that direction plus the random term accounting for multipath reception (relative to the average received level). However, in the practical case, it is not possible to separate between the path loss and shadowing loss. Therefore, the Radon projection accounts for the total loss along the propagation path. So, the sinogram matrix [6] forwarded to the reconstruction methods is defined by $\mathbf{G} = [\text{EIRP} - G_r + L_r - P_r(\rho_j, \theta_k)]_{j=1,\ldots,m;k=1,\ldots,n}$, where m is the number of samples per Radon projection and n is the number of projections.

D. Floor Maps

Fig. 2 shows the two maps used in the RF TWM simulations considered in this work. These maps represent 9.2×9.2 m^2 areas. At the center of each area there is an 8×8 m^2 room. All walls are assumed to be 50-cm thick and made of concrete without steel reinforcement rods. The floor maps are stored as 128×128 matrices, so each pixel corresponds to $9.2/128 \approx 7.2$ cm on the field.

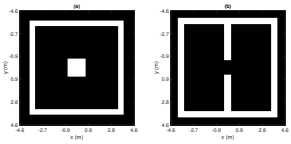

Fig. 2. Floor maps used in the simulations.

E. Sinogram Acquisition

To acquire the sinogram using a parallel-beam geometry, the transmitter and receiver pair moves along L-meter long lines. The receiver measures the mean received power with a $\Delta\rho$ spacing between subsequent samples. Therefore, the length of each Radon projection is

$$L = (m-1)\Delta\rho \tag{8}$$

where m is the number of samples per projection. Notably, for any given θ, L must be long enough to cover the whole area being mapped. The transmitter-receiver distance is also equal to L meters.

The samples collected along a line provide a discrete Radon projection. Radon projections were obtained at n angles uniformly spaced in [0,π), i.e., $\Delta\theta = \lfloor 180/n \rfloor$ degrees. Consequently, the full sinogram has $m \times n$ samples. To simulate lower sampling rates, proper subsets of the sinogram are selected.

The reconstructed images' sizes are $m \times m$ pixels, and they represent areas larger than the original floor maps. For example, to obtain a Radon projection of an 9.2×9.2 m^2 area at $\theta = 45$ degrees, $L \geq 9.2\sqrt{2} \approx 13$ meters. Therefore, the reconstructed images represent a 13×13 m^2 area. To compensate that and remove the excess length, the resulting images are cropped, such that their final size is $2\left(\left\lfloor \frac{m}{2\sqrt{2}} \right\rfloor \times \left\lfloor \frac{m}{2\sqrt{2}} \right\rfloor\right)$ pixels.

F. Operational Frequency Selection

Table I lists the RF propagation parameters of interest at 500, 1000 and 2000 MHz: (i) the offset, i.e., the loss at $d_0 = 1$ meter from the transmitting antenna [10]; (ii) the path loss exponent (attenuation slope) inside a typical office building [10]; (iii) the attenuation factor (specific attenuation) through concrete [11].

TABLE I
RF PARAMETERS AT 0.5, 1 AND 2 GHZ.

Frequency (MHz)	Offset (dB)	$\beta_{\text{slope,in}}$ (dB/decade)	Specific Attenuation through Concrete (dB/m)
500	26	36	36.0
1000	32	33	46.1
2000	38	30	57.5

The path loss exponent outside the building ($\beta_{\text{slope,out}}$) was assumed to be 20 dB/decade [12]. Table I indicates that the through-wall attenuation is more than 10 dB lower at 1 GHz than at 2 GHz. Furthermore, frequencies around 2 GHz are to be avoided due to the external interference posed by the WiFi, 3G and 4G cellular networks. At 500 MHz the 60-cm wavelength would result in high energy diffracted components. Pondering these issues, frequencies around 1 GHz were selected for the simulations.

III. Selecting an Objective Comparison Metric

The selected metric should **(i)** not be very sensitive to noise in the reconstructed image; **(ii)** compare the similarity of the objects' shape in the image, and not only pixel misclassification rate; and **(iii)** follow as closely as possible the subjective evaluation of the reconstruction quality.

Metrics that just measure the pixel misclassification rate, such as mean-squared error or sum of absolute distances, would report a high distance between two images if one or more boundaries in one of them are just slightly shifted. This would happen even if such shifting preserved the shape of the objects in the image. To avoid that, we selected the Mean Structural Similarity Index (MSSIM) [13]. The MSSIM is the average of the Structural Similarity Index (SSIM) values, which are calculated within a sliding window that is shifted pixel by pixel throughout the whole image. The SSIM is based on the assumption that human visual perception is specialized for the extraction of structural information from an image. The SSIM is given by

$$\text{SSIM}_i\left(f_i, \hat{f}_i\right) = \left[l\left(f_i, \hat{f}_i\right)\right]^{(1/a_1)} \left[c\left(f_i, \hat{f}_i\right)\right]^{(1/a_2)} \left[s\left(f_i, \hat{f}_i\right)\right]^{(1/a_3)} \tag{9}$$

where f_i and $\hat{f}_i$ are the contents of the original and reconstructed image at the ith local window; functions l, c and s are defined in [13] and account for the luminance, contrast and structural similarities, respectively. Their outputs lie within $[0, 1]$. Positive parameters a_1, a_2 and a_3 adjust the relative weights of the three components. The MSSIM index is then provided by

$$\text{MSSIM}\left(f_i, \hat{f}_i\right) = \frac{1}{M}\sum_{i=1}^{\text{M}} \text{SSIM}_i\left(f_i, \hat{f}_i\right) \tag{10}$$

where M is the number of local windows in the image. To calculate the SSIM, both $f(x, y)$ (the original image) and $\hat{f}(x, y)$ (the reconstructed image) must have the same dimensions, and their luminance values must be normalized to the same range. The MSSIM was calculated using $\frac{2}{3}\left(\left\lfloor \frac{m}{2\sqrt{2}} \right\rfloor \times \left\lfloor \frac{m}{2\sqrt{2}} \right\rfloor\right)$ local windows, with $a_1 = 1$, $a_2 = 2$ and $a_3 = 4$.

IV. Simulation Results

For all simulations, $G_t = G_r = 14$ dBi (isotropic gain of transmitter and receiver antennas), $L_t = L_r = 3$ dB (cable and connector losses at the transmitter and at the receiver) and $P_t = 40$ dBm (transmitter output power). In subsection IV-C, the receiver sensitivity (S_0) varies to allow evaluation of projection clipping in the reconstruction. In all other subsections, $S_0 = -110$ dBm. Furthermore, $L = 13$ meters and $m = 256$ samples per projection. Rearranging the terms in equation (8), one gets an inter-sample distance $\Delta\rho = L/(m-1) = 5$ cm. The histograms of all reconstructed images have been equalized for contrast enhancement and better visualization. FBR and DFR employed linear interpolation.

A. ART and SIRT Convergence

Fig. 3 shows the convergence of algebraic methods ART and SIRT [15] with $n = 80$ projections when applied to the reconstruction of the floor maps depicted in Fig. 2. A vector with all elements set to zero has been arbitrarily chosen as the initial solution of both iterative methods. The convergence is expressed as a function of the similarity between the original and reconstructed images, calculated using the MSSIM. The behavior presented by both ART and SIRT is typical of regularization methods which show *semi-convergence* [3]. Notably, ART reaches the optimal solution in the first iteration, which can be explained by a geometric interpretation of Kaczmarz's

method: the greater the angle between the hyperplanes defined by adjacent lines of **A**, the faster the algorithm converges to the optimal solution. If the hyperplanes defined by adjacent lines of **A** are nearly orthogonal, then the algorithm might converge in just one iteration [7]. In the reconstruction problem analyzed in this section, due to **A**'s sparsity (only 0.49% of non-null elements), this condition is observed (most angles lie in the interval $[84.9, 90]$ degrees range).

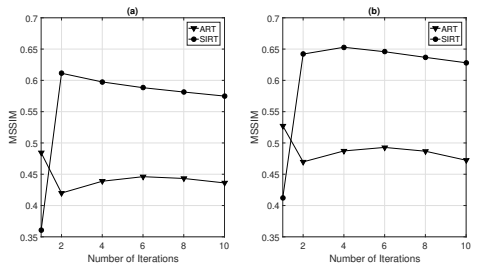

Fig. 3. ART and SIRT convergence (averaged over 100 runs) in the reconstruction of floor maps (a) 1 and (b) 2.

Fig. 4 displays the ART and SIRT reconstruction of floor maps 1 and 2. The behavior described by the MSSIM curves in Fig. 3 is observed in the ART and SIRT images: (i) ART with four iterations is slightly noisier than with one iteration, as Figs. 4a,b and Figs. 4e,f indicate; this is typical of the semi-convergence [3] inherent to regularization techniques such as ART, where, as the number of iterations increase after a certain point, noise starts to dominate the output; (ii) SIRT greatly improves when the number of iterations rises from one to four: with only one iteration, SIRT reconstructed images are considerably blurred, as Figs. 4c,g show; with four iterations that blurring is greatly reduced, as Figs. 4d,h indicate.

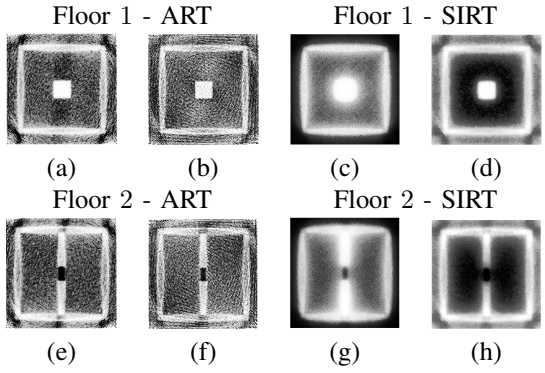

Fig. 4. Reconstructed floor maps 1 and 2: ART with 1 (a,e) and 4 (b,f) iterations; SIRT with 1 (c,g) and 4 (d,h) iterations.

In all simulations in the remaining sections, the number of iterations used in ART and SIRT is one and four, respectively.

B. Reconstruction Quality versus Number of Projections

Fig. 5 shows the MSSIM of the reconstructed floor maps for all methods as a function of n. Fig. 5a refers to floor map 1 and Fig. 5b to floor map 2. In both cases, FBR, DFR [16], and SIRT MSSIM increase with n. However, the MSSIM increment is negligible when n rises from 40 to 80 projections. This can be verified comparing Fig. 6d ($n = 40$) and Fig. 4d ($n = 80$), which show SIRT reconstructions of floor map 1: they are quite similar. The same applies to Fig. 6h ($n = 40$) and Fig. 4h ($n = 80$), which illustrate SIRT reconstructions of floor map 2.

Some degree of aliasing is inevitable in the reconstructed maps, as the original images are not band-limited. However, for a lower number of projections, the aliasing artifacts become more evident, as Fig. 7 shows. Despite that, the reconstructed floor maps are still recognizable with only 10 projections.

The MSSIM curves in Fig. 5 indicate that DFR has the worst performance. This can be promptly confirmed observing Fig. 6f ($n = 40$) and Fig. 7f ($n = 10$), where DFR fails to clearly reproduce a key feature of floor map 2: the door interconnecting the two rooms.

Finally, Fig. 5 shows that ART MSSIM has an "anomalous" behavior: it decreases as n augments. Comparing Fig. 6c and Fig. 7c (floor map 1), one sees that for $n = 40$ there is more "background" noise in the ART reconstructed image. The same applies when comparing Fig. 6g and Fig. 7g (floor map 2). This effect can be understood through the fact that lowering the number of samples results in low pass filtering. This reduces the high-frequency noise due to multipath. However, details of the floor maps are also lost. In fact, with $n = 10$, the aliasing artifacts corrupt the image significantly. Therefore, in that particular case, MSSIM failed to follow the subjective image quality evaluation.

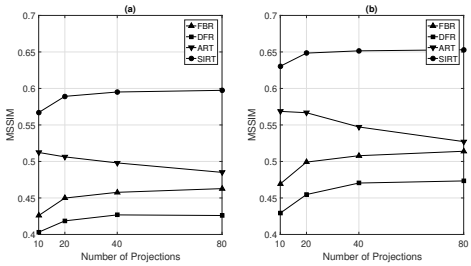

Fig. 5. MSSIM (averaged over 100 runs) versus number of projections in the reconstruction of floor maps (a) 1 and (b) 2.

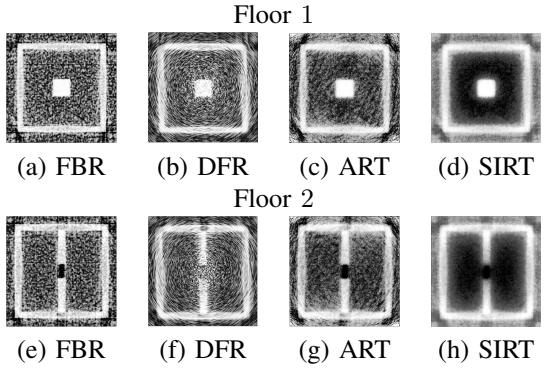

Fig. 6. Reconstruction of floor maps 1 and 2 ($n = 40$).

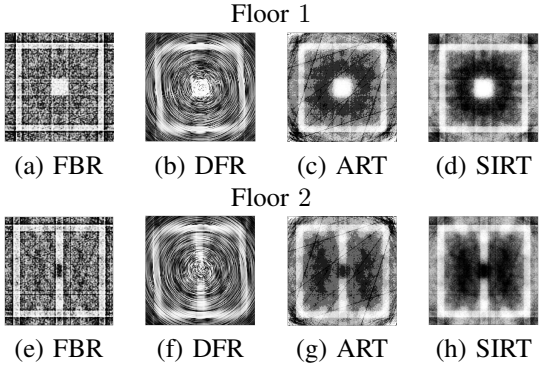

Fig. 7. Reconstruction of floor maps 1 and 2 ($n = 10$).

C. Effect of Projection Clipping on Reconstruction Quality

All previously reconstructed images in this work were obtained for a maximum supportable over-the-air path loss of $L_{\max} = 172$ dB. This resulted in only 1.4% and 3.0% of clipped samples in floor maps 1 and 4, respectively. To better assess the effect of projection clipping on reconstruction quality for all methods, this section evaluates the MSSIM as a function of $L_{\max}$. To increase the value of $L_{\max}$ from 172 dB down to 92 dB, the receiver sensitivity rose from -110 dBm up to 10 dBm. Fig. 8 displays the results for both floor maps. SIRT clearly outperforms all other evaluated methods for all values of $L_{\max}$. However, as the receiver is desensitized, SIRT's quality approaches that of FBR.

Table II informs the percentage of clipped samples at each floor map for each value of $L_{\max}$. For $L_{\max} \leq 92$ dB, the floors features cannot be recognized on the reconstructed images. That is why MSSIM for all methods (except ART) falls just slightly when $L_{\max}$ decreases from 92 dB to 52 dB.

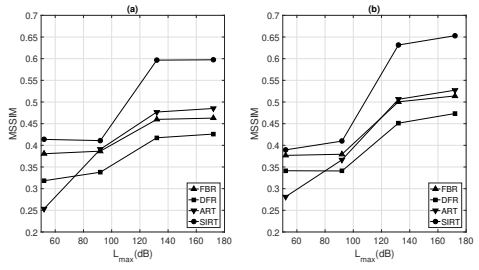

Fig. 8. MSSIM (averaged over 100 runs) versus $L_{\max}$ in the reconstruction of floor maps (a) 1 and (b) 2.

TABLE II

PERCENTAGE OF CLIPPED SAMPLES FOR DIFFERENT VALUES OF $L_{\max}$.

$L_{\max}$ (dB)	Percentage of clipped samples	
	Floor 1	Floor 2
172	1.4%	3.0%
132	12%	19%
92	55%	67%
52	80%	83%

V. CONCLUSIONS

This work conducted a comparative evaluation of the quality of reconstructed images provided by four methods originally applied in X-ray CTI: FBR, DFR, ART, and SIRT. For that, a path-loss model was defined to simulate RF propagation. The offset and slope coefficients were empirically defined, using values published in the literature for typical office buildings. The equations were corrupted by Rayleigh noise, to emulate the effect of multipath reception. Besides that, projection clipping due to receiver's limited sensitivity was also considered.

The simulations show the superiority of SIRT quality in the intended RF application. The Landweber's regularization [7] mitigates noise more efficiently than ART, at the expense of a slightly longer convergence. In fact, ART, due to the quasi-orthogonality of the hyperplanes defined by the system matrix, converges in only one iteration. DFR reconstruction had the worst performance for any number of projections, failing to clearly identify a key feature in floor map 2: the door interconnecting two rooms. MSSIM provided an objective quality metric for the reconstructed images comparison, and, for the most part, followed the subjective evaluation closely.

REFERENCES

[1] M. Bjorkbom et al, "Localization Services for Online Common Operational Picture and Situation Awareness", *IEEE Access*, pp. 742–757, vol. 1, 2013.

[2] M. R. Endsley, "Towards a Theory of Situation Awareness in Dynamic Systems", *Human Factors: The Journal of the Human Factors and Ergonomics Society*, vol. 1, n. 37, pp. 32–64, 1995.

[3] P. C. Hansen, *Discrete Inverse Problems: Insight and Algorithms*, 1st ed., Society for Industrial and Applied Mathematics, Philadelphia, USA, 2010.

[4] Y. Mostofi and A. Gonzalez-Ruiz, "Compressive cooperative obstacle mapping in mobile networks", in *Proceedings of Military Communications Conference, 2010*, pp.524–530, Oct 2010.

[5] A. C. Kak and M. Slaney, "Principles of Computerized Tomographic Imaging", IEEE Press, 1st ed., 1988.

[6] R. C. Gonzalez and R. E. Woods, "Digital Image Processing", Pearson Prentice Hall, 3rd ed., 2008.

[7] Richard C. Aster and Brian Borchers and Clifford H. Thurber, "Parameter Estimation and Inverse Problems", Elsevier Academic Press, 1st ed., 2005.

[8] D. Puccinelli and M. Haenggi, "Multipath Fading in Wireless Sensor Networks: Measurements and Interpretation", *Proceedings of the 2006 International Conference on Wireless Communications and Mobile Computing*, pp. 1039–1044, Vancouver, Canada, 2006.

[9] J. Turkka M. Renfors, "Path loss measurements for a non-line-of-sight mobile-to-mobile environment", in *Proceedings of the 8th International Conference on ITS Telecommunications (ITST 2008)*, pp. 274–278, Oct 2008.

[10] International Telecommunications Union, "Propagation Data and Prediction Models for the Planning of Indoor Radiocommunication Systems and Radio Local Area Networks in the Frequency Range 900 MHz to 100 GHz", *Recommendation ITU-R P.1058-1*, 1997.

[11] C. D. Taylor et al, "Measurement of RF Propagation into Concrete Structures over the Frequency Range 100 MHZ to 3 GHz", *Wireless Personal Communications*, v. 377, pp.131–144, 1997.

[12] C. Perez-Vega and Jose Luis Garcia and Jose Miguel Lopez Higueraz, "A simple and efficient model for indoor path-loss prediction", *Meas. Sci. Technol.*, vol.8, pp.1166–1173, 1997.

[13] Z. Wang et al, "Image Quality Assessment: From Error Visibility to Structural Similarity", *IEEE Transactions on Image Processing*, vol.13, n.4, pp.600–612, apr 2004.

[14] W. L. Martinez and A. R. Martinez, "Computational Statistics Handbook with MATLAB", 1st Edition, Chapman and Hall/CRC, 2012.

[15] Per Christian Hansen and Maria Saxild-Hansen, "AIR Tools - A MATLAB package of algebraic iterative reconstruction methods", Journal of Computational and Applied Mathematics, vol. 236, n. 8, pp. 2167 – 2178, 2012.

[16] Chang Yiu Chuen Lewis, "Central Slice", 2011. [Online]. Available: http://code.google.com/archive/p/centralslice/.